Angle-resolved optically detected magnetic resonance as a tool for strain determination in nanostructures

A. Bogucki ●,[1,*] M. Goryca ●,[1] A. Łopion ●,[1] W. Pacuski ●,[1] K. E. Połczyńska ●,[1] J. Z. Domagała ●,[2] M. Tokarczyk ●,[1] T. Fąs ●,[1] A. Golnik ●,[1] and P. Kossacki ●[1]

[1]*Institute of Experimental Physics, Faculty of Physics, University of Warsaw, Pasteura 5, 02-093 Warsaw, Poland*
[2]*Institute of Physics, Polish Academy of Sciences, Aleja Lotników 32/46, 02-668 Warsaw, Poland*

In this paper, we apply the angle-resolved optically detected magnetic resonance (ODMR) technique to study a series of strained (Cd, Mn)Te/(Cd, Mg)Te quantum wells (QWs) produced by molecular beam epitaxy. By analyzing characteristic features of ODMR angular scans, we determine the strain-induced axial-symmetry spin Hamiltonian parameter D with neV precision. Furthermore, we use low-temperature optical reflectivity measurements and x-ray diffraction scans to evaluate the local strain present in the QW material. In our analysis, we take into account different thermal expansion coefficients of the GaAs substrate and CdTe buffer. The additional deformation due to the thermal expansion effects has the same magnitude as the deformation that originates from the different compositions of the samples. Based on the evaluated deformations and values of the strain-induced axial-symmetry spin Hamiltonian parameter D, we find the strain spin-lattice coefficient $G_{11} = (72.2 \pm 1.9)$ neV for Mn^{2+} in CdTe and shear deformation potential $b = (-0.94 \pm 0.11)$ eV for CdTe.

I. INTRODUCTION

One of the critical factors influencing the electronic and optoelectronic devices' performance is local strain distribution. For example, the spin relaxation time—a crucial parameter for potential spintronic devices—strongly depends on spin-lattice coupling and local strain distribution. The latter is particularly nontrivial in complex nanostructures composed of many different materials, e.g., in quantum wells (QW). Such structures can be produced with several different growth techniques like metalorganic vapor-phase epitaxy (MOVPE) or molecular beam epitaxy (MBE). Historically, the development of semiconductors' growth methods was accompanied by independent improvement of materials characterization techniques, which resulted in a comprehensive knowledge foundation for future research and advanced applications. Naturally, new characterization techniques combined with new growth methods offer fresh insights into semiconductor physics and often shed new light on some previously determined material parameters. For example, this was the case of GaAs crystals widely used as substrates for complex semiconductor structures. In 1959, Kolm *et al.* [1] used x-ray diffraction to determine the lattice constant of the GaAs crystals produced with the Bridgman-Stockbarger method. However, crystals grown nowadays with the use of other techniques like horizontal Bridgman (HB), liquid encapsulated Czochralski (LEC), vertical gradient freeze (VGF), or epitaxial methods resulting in different concentrations of impurities systematically exhibit different lattice constants [2,3].

Finding a particular material parameter for materials obtained by a specific growth method is critical for real multilayer devices. Determining some structural parameters is particularly challenging in small-volume structures (e.g., single QWs). A small amount of material often excludes many characterization techniques like x-ray diffraction, which is a standard method of measuring the strain in semiconductor nanostructures. A possible solution to this issue is an incorporation of a small amount (below 1%) of magnetic ions into the structure and determination of local strain exploiting the coupling between those ions and the strain of the crystal lattice. In many cases (like multiple QWs structures), determining the spin Hamiltonian parameters describing such coupling may be done with electron paramagnetic resonance (EPR) techniques [4]. However, in thin structures, the number of spins is insufficient to produce a detectable EPR signal. This problem can be overcome by using the optically detected magnetic resonance (ODMR) technique which exploits the strong exchange interaction between magnetic ions and photogenerated carriers and facilitates detection of the paramagnetic resonance of a significantly smaller amount of magnetic ions.

In this paper, we present a comprehensive analysis of the local strain present in a series of (Cd, Mn)Te/(Cd, Mg)Te QWs. We combine data obtained from angle-resolved ODMR, low-temperature reflectance measurements, and x-ray diffraction scans. The scheme presented in Fig. 1 shows how we address the problems formulated in the previous paragraph. We design a series of (Cd, Mn)Te/(Cd, Mg)Te quantum well samples fabricated by the MBE method that have different
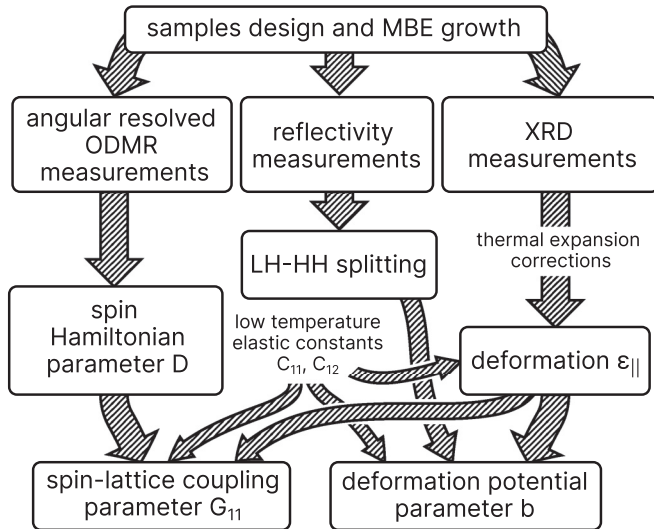
---

*Aleksander.Bogucki@fuw.edu.pl

FIG. 1. The schematic overview of this work. There are three main branches related to the experimental techniques used in this paper: angular-resolved ODMR measurements, reflectivity measurements, and XRD measurements. By combining the results of these methods, we determine the spin-lattice coupling parameter G_{11} and deformation potential parameter b for the Mn^{2+} ion in CdTe.
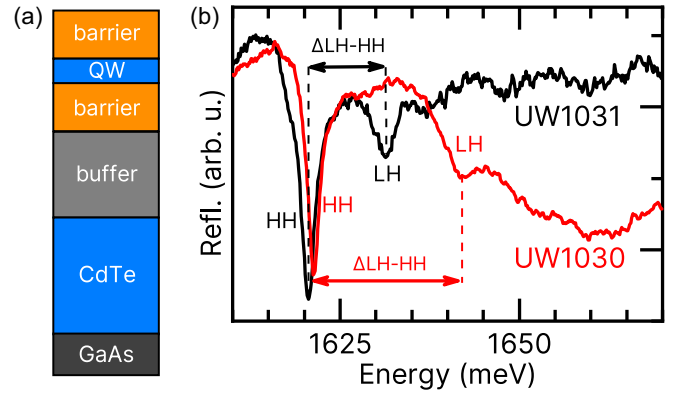

FIG. 2. (a) A schematic of a representative sample structure used in the whole sample series used in this article. The buffer layer was made of (Cd, Mg)Te where magnesium content was varying from 0% up to approx. 30%. Barriers were made of (Cd, Mg)Te while the quantum well (QW) was made of (Cd, Mn)Te with manganese concentration below 0.5%. (b) Reflectivity spectra of two example samples. Sample UW1030 has a higher concentration of magnesium in the buffer layer than UW1031 and thus exhibits larger strain, which results in larger energy splitting between heavy-hole exciton (HH) and light-hole exciton (LH).

deformation in the QW layer by design. The QW material is doped with a small amount of manganese (<1%) which exhibits paramagnetic resonance. Using angle-resolved ODMR, we determine the strain-induced axial-symmetry spin Hamiltonian parameter (D) with high accuracy. Independently, we perform XRD measurements on the least and the most strained samples—as only for these samples the XRD method yields a reliable deformation value. After considering the additional deformation that originates from the different thermal expansion coefficients of the substrate and QW material, we deduce the deformation values for all samples. To check if other samples also follow the design scheme, we perform low-temperature reflectivity measurements. We determine the energy splitting between light-hole (LH) exciton transition and heavy-hole (HH) exciton transition from reflectivity spectra. We find that the HH-LH splitting for the whole series of samples exhibits monotonic behavior—thus validating the designed distribution of deformation. As the ODMR measurements are taken at cryogenic temperatures, we evaluate the CdTe elastic stiffness constants C_{11} and C_{12} at 1.6 K from available literature data. Then, from the obtained deformation values and the corresponding strain-induced axial-symmetry spin Hamiltonian parameter D combined with the elastic constants, we calculate the spin-lattice coupling coefficient G_{11} for manganese in cadmium telluride. The spin-lattice coupling coefficient G_{11} value obtained in this work diverges from previously reported in Ref. [5]. Furthermore, we use HH-LH splittings and deformation data to find the deformation potential b. The obtained value of b is similar to Ref. [6] one but different from the values reported in Refs. [7–9]. Our findings could be especially useful in all studies involving spin-related phenomena in CdTe-based MBE-grown nanostructures and devices including multiple-QWs and quantum dots [10–28].

II. EXPERIMENT AND RESULTS

A. Samples

The samples containing QWs used in this work were produced by the molecular beam epitaxy (MBE) technique. An illustration of the samples is presented in Fig. 2(a). In order to obtain structures with a different strain, we have changed the content of magnesium in the buffer layer and the barrier layer (see Table I). The magnesium content was deduced based on magnesium fluxes and calibration obtained by the reflectance measurements [29,30]. The nominal width of (Cd, Mn)Te QW was 10 nm. The value of the QW width was chosen to ensure sufficient confinement together with narrow excitonic features in the reflectivity spectra, as well as being well below the critical thickness of the CdTe lattice relaxation [31,32]. The manganese content was determined by magnetooptical measurements of the giant Zeeman splitting and fitting the modified Brillouin function [33]. The thickness of the (Cd,

TABLE I. The composition of samples used in this article, the deformation present in the QW calculated for 300 K without correction for different thermal expansion coefficients of CdTe and GaAs, and the deformation present in the QW calculated for 1.6 K with thermal-expansion-coefficient-difference correction.

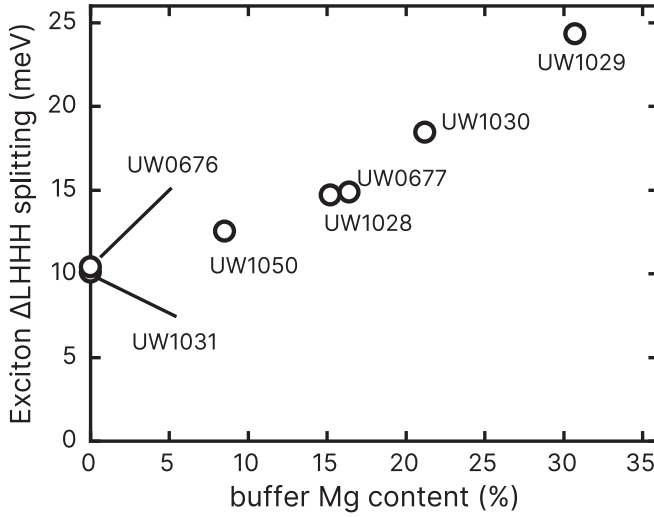| Sample no.	Buffer Mg (%)	Barrier Mg (%)	QW Mn (%)	$\varepsilon_{\parallel}^{T=300\ K}$ w/o corr. (‰)	$\varepsilon_{\parallel}^{T=1.6\ K}$ corr. (‰)
UW1029	30.7	30.7	0.30	−2.870	−3.512
UW1030	21.2	21.2	0.31	−1.959	−2.601
UW1028	16.4	16.4	0.14	−1.538	−2.180
UW0677	15.2	15.2	0.26	−1.396	−2.038
UW1050	8.5	16.4	0.15	−0.780	−1.422
UW1031	0	21.2	0.26	0.058	−0.584
UW0676	0	17.3	0.27	0.060	−0.582

FIG. 3. The energy difference between the lowest light-hole excitonic state and the lowest heavy-hole excitonic state (ΔLHHH splitting) plotted vs magnesium content in the buffer layer for all samples from Table I confirms that the growth process was fully controlled.

Mg)Te barriers was 50 nm, the (Cd, Mg)Te buffer layer was 2000 nm (far above the critical thicknesses of the (Cd, Mg)Te [34]), and the additional CdTe layer below the buffer was 4000 nm thick. This additional layer ensured the isolation from the GaAs substrate. To confirm that we obtained the designed strain in the produced samples, we have performed reflectivity measurements [see Fig. 2(b)]. The identification of the spectrum features was based on standard magneto-optical measurements (not shown) [35–37]. The energy splitting between light-hole exciton and heavy-hole exciton visible in spectroscopic measurements is a linear function of the strain present in the QW layer [6,38–40]. Therefore, as the samples are similarly designed, the light-hole heavy-hole splitting gives a hint about the existing strain.

Figure 3 shows heavy-hole exciton light-hole exciton splitting obtained as a function of magnesium content in the buffer layer for all samples. The monotonic behavior of extracted data confirms that the samples follow the design—the higher the magnesium content, the larger the light-hole heavy-hole splitting.

B. XRD measurements

In order to independently calibrate deformation, we have performed room-temperature x-ray diffraction (XRD) measurements of the two extreme samples: UW1029 (highest strain) and UW1031 (lowest strain)—see Fig. 4. By analyzing the 004 and the $\overline{3}\overline{3}5$ reflections, we extract the lattice constants of CdTe separation layer (about $a = 6.481$ Å) and the strained layers. Throughout this work, for the calculations we use the following lattice constants of pure materials at room temperature: $a_{CdTe} = 6.481$ Å [41], $a_{MnTe} = 6.337$ Å [42], $a_{MgTe} = 6.419$ Å [29], and $a_{GaAs} = 5.6535$ Å [43]. The obtained results agree with the sample design.

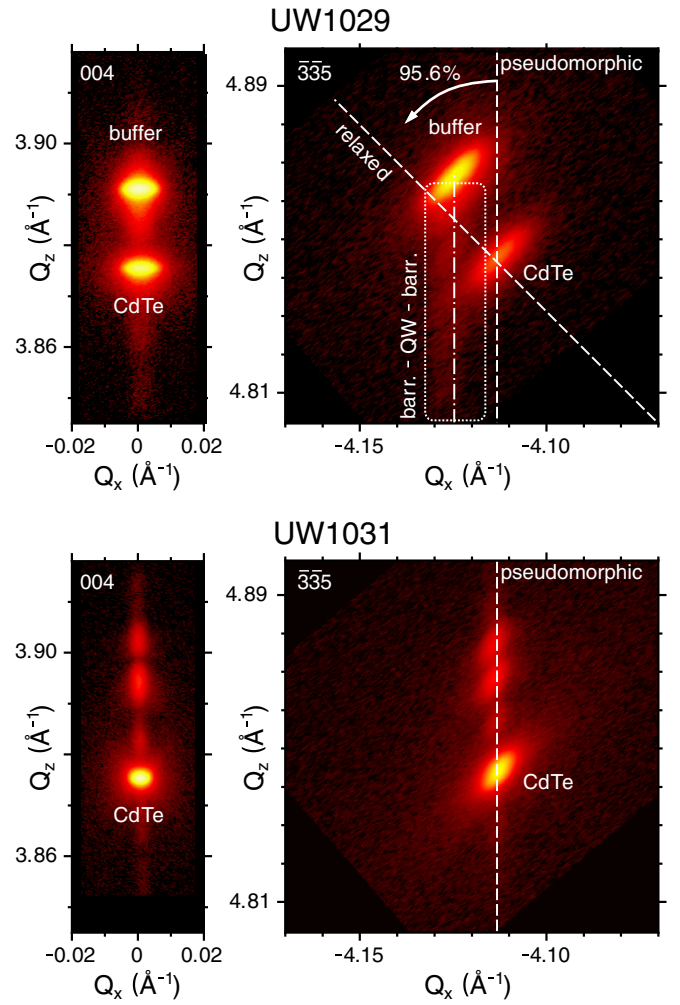FIG. 4. The top panel shows XRD reciprocal space maps of 004 (left) and $\overline{3}\overline{3}5$ (right) reflections obtained for a high-strain sample (UW1029). There are two strong peaks attributed to CdTe and to (Cd, Mg)Te buffer layer. Analysis of $\overline{3}\overline{3}5$ map confirms that the strain in the QW is induced by the buffer layer, as weak satellite peaks are present along the vertical line meaning pseudomorphic growth with a buffer lattice constant (dotted rectangle). The bottom panel presents maps from the same region of reciprocal space (left: the 004 reflection, right: the $\overline{3}\overline{3}5$ reflection) for the low-strain sample (UW1031). All peaks present in the $\overline{3}\overline{3}5$ map appear along the horizontal line above the CdTe peak, confirming the pseudomorphic character of growth with the CdTe lattice constant.

In XRD maps of the high-strain sample (UW1029), there are two strong reflections—one corresponding to the 4 μm CdTe layer, and the second one to 2 μm (Cd, Mg)Te buffer layer. Positions of the reflections give the lattice constants of CdTe and buffer at room temperature (where $\parallel$ and $\perp$ denote directions parallel and perpendicular to the samples surface, respectively): $a_{\parallel}^{CdTe} = (6.4807 \pm 0.0006)$ Å, $a_{\perp}^{CdTe} = (6.4862 \pm 0.0001)$ Å, $a_{\parallel}^{buff} = (6.4616 \pm 0.0003)$ Å, and $a_{\perp}^{buff} = (6.4595 \pm 0.0001)$ Å. From these values and using the formula

$$a_{relax} = (C_{11}a_{\perp} + 2C_{12}a_{\parallel})/(C_{11} + 2C_{12}),$$
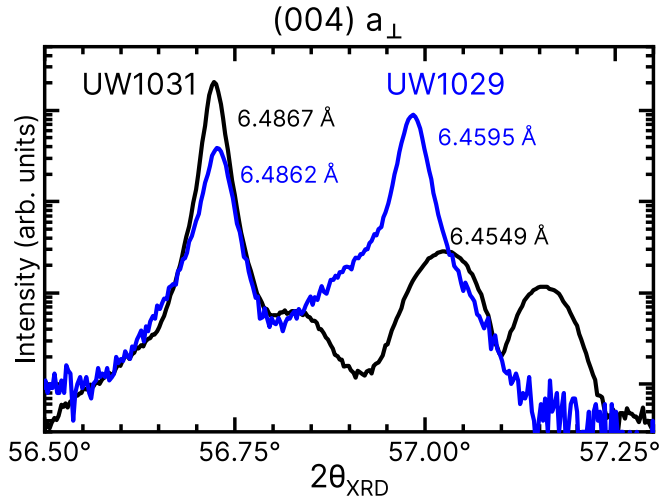
FIG. 5. The $2\theta/\Omega$ XRD scan of the 004 reflection for low-strain (UW1031, black line) and high-strain (UW1029, blue line) samples. Lattice constants calculated from this measurement combined with values obtained from asymmetric reflection $\bar{3}35$ confirm that the obtained strain agrees with the designed one.

FIG. 6. The energy difference between the lowest light-hole excitonic state and the lowest heavy-hole excitonic state (ΔLHHH splitting) plotted as a function of deformation $\varepsilon_\parallel$ at 1.6 K for analyzed quantum well samples. The empty circles represent measured data and the black crosses are the results of numerical simulations described in Appendix II B. The black line is a result of a linear fit to the data points. The shear deformation potential $b = (-0.94 \pm 0.11)$ eV is calculated from the slope of an obtained line [Eq. (1)].

we can calculate the lattice constant of the relaxed material and finally obtain the deformation of the buffer layer $\varepsilon_\parallel = -0.3565‰$. The fact that the nominally relaxed material has nonzero deformation is explained in the following sections. The coefficients C_{12} and C_{11} are the elastic stiffness constants of CdTe. More details about the evaluation of elastic stiffness constants at different temperatures are provided in Appendix. The analysis of the $\bar{3}35$ reflection shows that the buffer layer is not fully relaxed. The relaxation degree of the buffer layer in the UW1029 sample is 95.6%.

The situation is easier to interpret in the case of the low-strain sample (UW1031), where on top of the separation layer made of CdTe there is a buffer layer also made from CdTe. In principle, the lattice constant of the thin, strained barrier (thickness well below critical thickness) should be matched to the lattice constant of the thick CdTe buffer. Therefore the lattice constant of the QW should be close to the parallel lattice constant of CdTe. The obtained values of lattice constants for the UW1031 sample from XRD measurements are $a_\parallel^{\text{CdTe+buffer}} = (6.4807 \pm 0.0006)$ Å, $a_\perp^{\text{CdTe+buffer}} = (6.4867 \pm 0.0001)$ Å, $a_\parallel^{\text{2nd}} = (6.4797 \pm 0.0008)$ Å, $a_\perp^{\text{2nd}} = (6.4549 \pm 0.0001)$ Å, where the superscript 2nd denotes the second strongest peak and is related to the signal close to the $\approx 57°$ in the $2\theta/\Omega$ XRD scan (see Fig. 5). From this, we can calculate $\varepsilon_\parallel = -0.389‰$, which in the case of the UW1031 sample is also the deformation present in the QW at room temperature.

The influence of temperature is critical in the correct determination of deformation in heterogenic structures [44–47], which is the case of our sample, as the used materials exhibit different temperature expansion coefficients. There are three distinctive temperature points that should be considered in the context of this work. (i) The growth temperature at which CdTe layers were deposited in MBE. We have estimated this temperature to be 552 K—see Appendix. (ii) The room temperature (300 K) at which XRD measurements
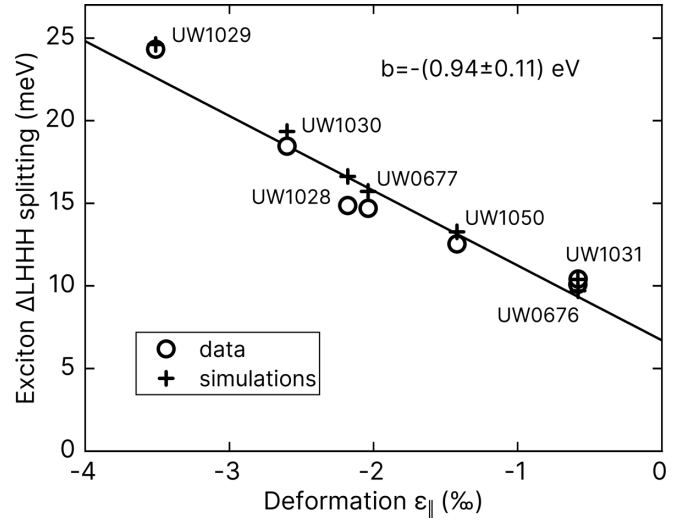
were taken. During the cooling after the growth process, an additional compressive deformation builds up in the QW layer, as the GaAs substrate shrinks more than CdTe during the cooling. So at room temperature there is an additional deformation originating from the different shrinking of the QW layer and the substrate layer that is visible in XRD measurements: $\varepsilon_\parallel^{552\,\text{K}\to300\,\text{K}} = -0.389‰$. (iii) The pumped liquid helium temperature ($\approx$1.6 K) at which reflectivity and ODMR measurements were performed. The GaAs temperature expansion coefficient differs from that of the CdTe (see Fig. 13 in Appendix). Moreover, the magnitude of that difference changes as the temperature decreases, finally resulting in an additional compression which gives contribution to the deformation $\varepsilon_\parallel^{300\,\text{K}\to1.6\,\text{K}} = -0.253‰$. Taking into account all of those contributions up together with starting value $\varepsilon_{\parallel\,\text{w/o corr.}}^{T=300\,\text{K}} = 0.058‰$, we finally obtain the deformation in the CdTe QW layer at 1.6 K for the UW1031 sample, $\varepsilon_\parallel = -0.584‰$.

Now, using the above calibration and taking into account an additional temperature-originating deformation, it is possible to present the light-hole-heavy-hole splitting as a function of deformation (Fig. 6). We obtain the band shear deformation potential $b = (-0.94 \pm 0.11)$ eV using the formula [48]

$$\Delta\text{LHHH} = 2b\left(1 + \frac{2C_{12}}{C_{11}}\right)\varepsilon_\parallel + \text{const.} \qquad (1)$$

The shear deformation potential obtained in this work is close to the value (-1.05 ± 0.01) eV obtained by Merle d'Aubigné *et al.* [6]. The other experimentally determined value is $b = 1.24$ eV by Thomas and coworkers [7]. Other values available are given by Peyla *et al.* [9], and by Mathieu *et al.* -1.4 eV [8]. However, the two latter ones are based on Refs. [7] and [6]. Namely, the value given by Peyla *et al.* [9] is
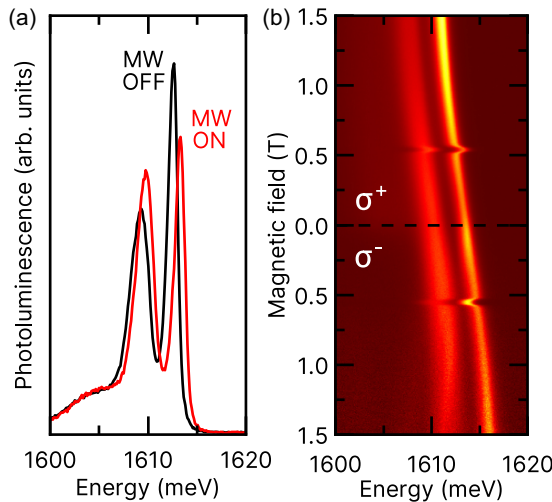
FIG. 7. (a) Photoluminescence (PL) spectra of (Cd, Mn)Te/(Cd, Mg)Te quantum well (QW) collected at 1.6 K at a magnetic field of 0.545 T with microwave radiation (15.3 GHz) turned on (red curve) and off (black curve). (b) Map of the normalized photoluminescence spectra of the same QW measured for various magnetic fields with microwave radiation present. The energetic position of the PL spectrum follows the modified Brillouin function, except the points at 0.545 T, where the paramagnetic resonance of Mn^{2+} ions placed in the QW occurs. As a result of the resonance, the giant Zeeman splitting rapidly decreases in those points.

the mean of values given by Thomas and Merle. The results of calculated light-hole–heavy-hole splitting obtained by numerically solving the finite QW model are marked in Fig. 6 with black crosses. More details about the QWs simulations are in Appendix.

C. Optically detected magnetic resonance measurements

Optically detected magnetic resonance is a technique that exploits the fact that the optical properties of the studied material change when paramagnetic resonance occurs. The microwave absorption at electron paramagnetic resonance (EPR) frequency leads to an increase of the Mn-system temperature, which results in a decrease of the optically detected magnetization [49–59]. The change in the optical properties of the sample can be detected with various experimental techniques. For example, previous ODMR studies of diluted magnetic semiconductors were based on changes in Faraday rotation [60], in the amplitude of photoluminescence, or in the spectral shift of the photoluminescence line [61–67]. In this work, we use the energy position of the neutral exciton emission line (X) from the photoexcited QW to detect the local magnetization in the QW layer (Fig. 7). For optical excitation, we use a $\lambda = 647$ nm laser (with a spot diameter of ≈ 100 μm) in a standard photoluminescence experimental setup. The sample is placed in the optical cryostat equipped with two perpendicular pairs of split superconducting coils. Thus, it is possible to obtain up to 3 T of a magnetic field in any direction in a given plane. In particular, it is possible to continuously change the magnetic field from the Faraday to Voigt configuration (scan over the out-of-plane angle θ in
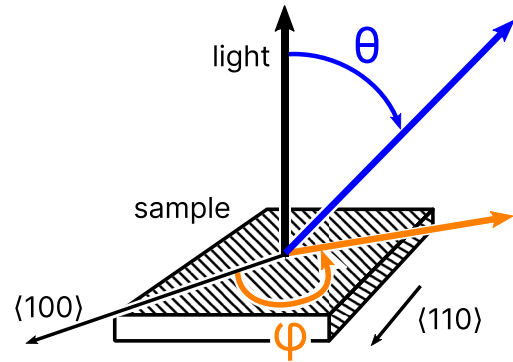

FIG. 8. Angles definition of the magnetic field directions. The sample edge is along $\langle 110 \rangle$ direction. The out-of-plane angle θ is the angle between the samples' growth axis and samples' surface. For example, $\theta = 0°$ means magnetic field along the growth axis in Faraday configuration, whereas $\theta = 90°$ means in-plane magnetic field. The in-plane angle φ is the angle between $\langle 100 \rangle$ direction and the direction of the magnetic field. The angle $\varphi = 45°$ means that the in-plane magnetic field was along $\langle 110 \rangle$ direction.

Fig. 8) or to rotate the magnetic field within the sample plane (scan over the in-plane angle φ in Fig. 8).

The representative photoluminescence spectrum (PL) for samples used in this work is presented in Fig. 7(a). The PL spectrum consists of two emission lines—at lower energies there is a line related to the charged exciton (CX) and at higher energies to the neutral exciton (X) [37]. During the scan in the magnetic field in Faraday configuration (magnetic field perpendicular to the surface of the sample and parallel to the optical axis) energetic position of X line can be described with the modified Brillouin function [33] (giant Zeeman effect). However, in the presence of microwave radiation, a paramagnetic resonance of manganese ions occurs at the resonant magnetic field, which results in a rapid decrease of giant Zeeman splitting [see Fig. 7(b) with its caption]. Comparison of PL spectra measured for a resonance magnetic field with and without microwave radiation are presented in Fig. 7(a). The difference in the energy position of X line for these two cases is called further in the text "the ODMR amplitude/signal." It is important to note that too strong laser excitation can alter the optical properties of QW resulting in a change of the position of the X line. To avoid this effect and ensure that the laser excitation does not influence the amplitude of the giant Zeeman splitting [68–71], we use the following procedure to determine an optimal laser excitation power. The magnetic field is set to the value of the paramagnetic resonance with microwave radiation turned off. The series of PL spectra are measured for decreasing laser power. The optimal laser power is a power that does not cause an energy shift of the neutral exciton emission line. In this work, the optimal laser power corresponds to the excitation density power $\rho < 0.005$ W/cm^2, which is even smaller than the low-power regime value presented in Ref. [68].

An example of representative ODMR signal as a function of magnetic field for fixed microwave frequency is presented in Fig. 9. The detailed features (multiple lines) visible in the ODMR spectrum originate from interactions of manganese
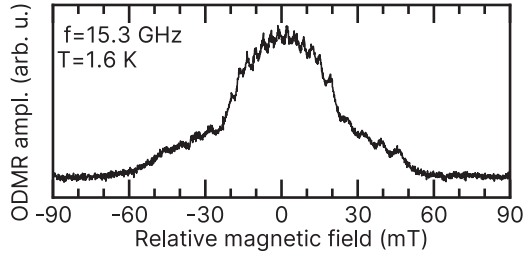
FIG. 9. Optically detected magnetic resonance (ODMR) signal of (Cd, Mn)Te/(Zn, Mg)Te quantum well obtained as a difference between the energetic position of the quantum well excitonic line with and without microwave radiation. The position with microwave radiation was directly extracted from measured spectra. The position without microwave radiation was established from the fitted modified Brillouin function. On the horizontal axis, we used the relative magnetic field—a magnetic field with a subtracted value of the resonance magnetic field for a given frequency of microwave radiation. The multiple features visible on the spectrum are originating from different terms of manganese Hamiltonian hyperfine structure interaction.

ion Mn^{2+} and CdTe material in QW and can be described with a spin Hamiltonian [4,72]:

$$\widehat{H} = g_{Mn}\mu_B \mathbf{\hat{B}\hat{S}} + A\mathbf{\hat{I}\hat{S}} + D\left[\hat{S}_z^2 - \frac{S(S+1)}{3}\right]$$
$$+ E\,R_z(\alpha)\left(\hat{S}_x^2 - \hat{S}_y^2\right)R_z^{-1}(\alpha)$$
$$+ \frac{a}{6}\left[\hat{S}_x^4 + \hat{S}_y^4 + \hat{S}_z^4 - \frac{S(S+1)(3S^2+3S-1)}{5}\right]. \quad (2)$$

The first term of the Hamiltonian is responsible for the Zeeman splitting (where g_{Mn} is the g factor of the manganese ion). The second one is a hyperfine coupling between the electronic spin and nuclear spin and it results in splitting the ODMR spectrum into six lines as the manganese 2+ ion has electronic spin $S = 5/2$ and nuclear spin $I = 5/2$. The third and fourth terms come from the electronic quadrupole fine structure present in less than cubic symmetry (strained QW) and can be written in a general form as $\hat{S}\mathbf{\hat{D}}\hat{S}$, where $\mathbf{\hat{D}}$ is a tensor. However, it can be reduced to only two parameters, D and E—the axial and rhombic zero-field splitting (ZFS) parameters (D is also called the strain-induced axial-symmetry parameter) [72]. The $R_z(\alpha)$ allows for the rotation of the reference frame around the growth axis of the QW. The last term describes the crystal-field splitting where a is the zero-field fine structure splitting parameter for the unstrained CdTe. As a consequence of the above Hamiltonian, the microwave absorption spectrum of Mn^{2+} ion consists of 30 transitions (five electronic spin transitions, each split into the sextet due to hyperfine interaction).

D. Angular-resolved ODMR

Angular-resolved ODMR measurements can give precise information about the spin Hamiltonian parameters D and E. While a single ODMR measurement in Faraday configuration should in principle give information about the D parameter, the angular ODMR can provide much more detailed information and increase experimental accuracy. The left panels of

Figs. 10 and 11 show the angular ODMR measurements of example high-strain and low-strain samples, respectively.

In the lower part of the plot, the angular scan from the Faraday configuration (magnetic field direction $\theta = 0°$) to the Voigt configuration (magnetic field direction $\theta = 90°$) is presented. The upper part of the plot shows an in-plane ODMR angular scan starting from $\langle 110 \rangle$ direction (parallel to the samples' edge) for $\varphi = 45°$. The whole ODMR angular map presents a set of characteristic features in which the location on the map allows for the determination of spin Hamiltonian parameters by comparison with similar numerically simulated maps (see the right panels).

The first characteristic feature is the width of the ODMR spectrum in Faraday configuration. In this configuration, a transition that is visible at the lowest magnetic field corresponds to the change of the electron spin projection from $S_z = +3/2$ to $S_z = +5/2$ with nuclear spin projection $I_z = +5/2$. Similarly, the transition at the highest magnetic field corresponds to the change of the electron spin projection from $S_z = -5/2$ to $S_z = -3/2$ with nuclear spin projection $I_z = -5/2$. The measure of splitting between the outermost lines in units of the magnetic field directly corresponds to the value of the D parameter in the spin Hamiltonian. At high magnetic field approximation—assuming that eigenstates are the same as the eigenstates of the z components of the spin operators, the spin Hamiltonian can be analytically solved. In such a case, the D parameter can be calculated as

$$D = (g_{Mn}\mu_B \Delta B_z - 5A - 4a)/8, \quad (3)$$

where ΔB_z is the distance in magnetic field units between the lowest and the highest transition lines in the ODMR signal.

The above expression enables the determination of the D parameter for $D \gtrsim 75$ neV. Below 75 neV, the transitions between other states are overlapping, and resolving the lines becomes cumbersome. The difference between D value calculated from Eq. (3) for 75 neV $< D < 1000$ neV and obtained by numerically solving the spin Hamiltonian for $f = 15.6$ GHz is below 0.05%. For higher values of D, the difference between the numerical solution and analytical approximation slowly increases but is still below 0.1% for D as high as 3000 neV.

Moreover, the positions of the ODMR signal line crossings in ODMR angular maps (like those present between $B \approx +20$ mT to $B \approx +30$ mT at $\theta \approx 30°$ and $\theta \approx 50°$ in Fig. 10 or in Fig. 11, marked with white arrows) enable for reducing fitting uncertainties down to a few neV. Similarly, by analyzing analogous features of an in-plane angular scan, we can fit the spin Hamiltonian E parameter, which in the case of QWs should be zero. Indeed, within fitting accuracy, the E parameter for our samples is negligible.

Figure 12 presents the obtained D parameter as a function of deformation. As it is known [4], the spin Hamiltonian D parameter is related to deformation $\varepsilon_\parallel$ by formula

$$D = -\frac{3}{2}G_{11}\left(1 + \frac{2C_{12}}{C_{11}}\right)\varepsilon_\parallel, \quad (4)$$

where G_{11} is the strain spin-lattice coefficient and C_{11}, C_{12} are elastic stiffness constants. The value of G_{11} strain spin-lattice
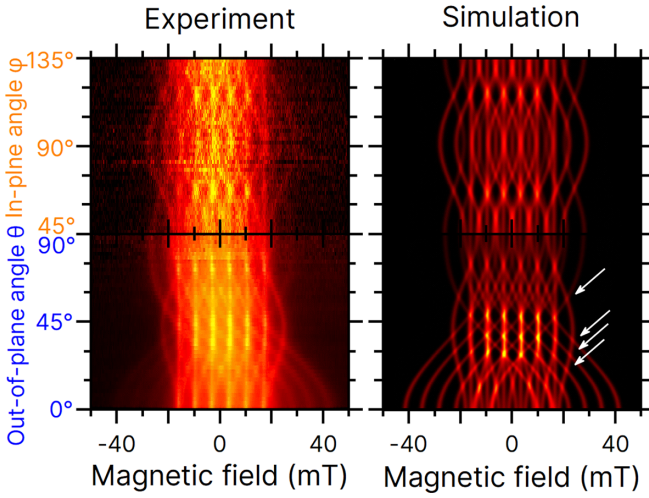
FIG. 10. The left panel shows the measured angular maps of the ODMR signal for the exemplary high-strain sample (UW0677). The intensity of the ODMR signal is coded in the brightness of the map. The upper left part (in-plane scan) was obtained for the fixed out-of-plane angle $\theta = 90°$. A lower left part (out-of-plane) scan was obtained for fixed in-plane angle $\varphi = 45°$. The right part presents results of simulations obtained by numerical solving of the spin Hamiltonian presented in Eq. (2) calculated for infinite temperature. Fitted spin Hamiltonian parameters are $D = (497 \pm 3)$ neV and $E = (-8 \pm 13)$ neV.

coefficient obtained from our data is $G_{11} = (72.2 \pm 1.9)$ neV. This is a significantly larger value than the only previously reported value [5] of $G_{11}^{\text{Causa}} = (57 \pm 1.3)$ neV.
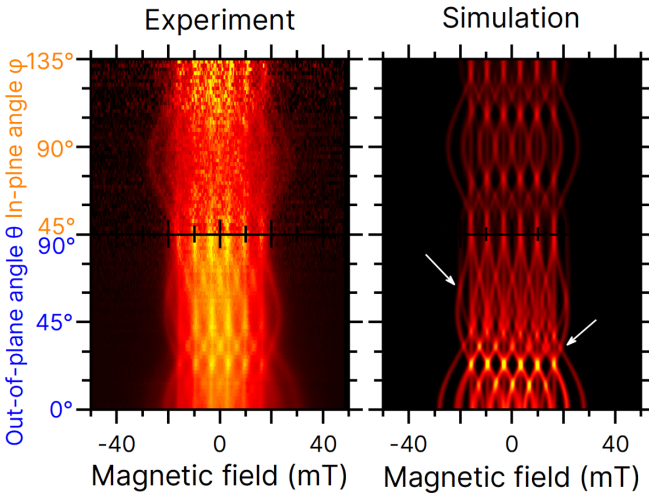

FIG. 11. The left panel shows the measured angular maps of the ODMR signal for the exemplary low-strain sample (UW0676). The intensity of the ODMR signal is coded in the brightness of the map. The upper left part (in-plane scan) was obtained for fixed out-of-plane angle $\theta = 90°$. A lower left part (out-of-plane) scan was obtained for fixed in-plane angle $\varphi = 45°$. The right part presents results of simulations obtained by numerical solving of the spin Hamiltonian presented in Eq. (2) calculated for infinite temperature. Fitted spin Hamiltonian parameters are $D = (155 \pm 3)$ neV and $E = (0 \pm 25)$ neV.
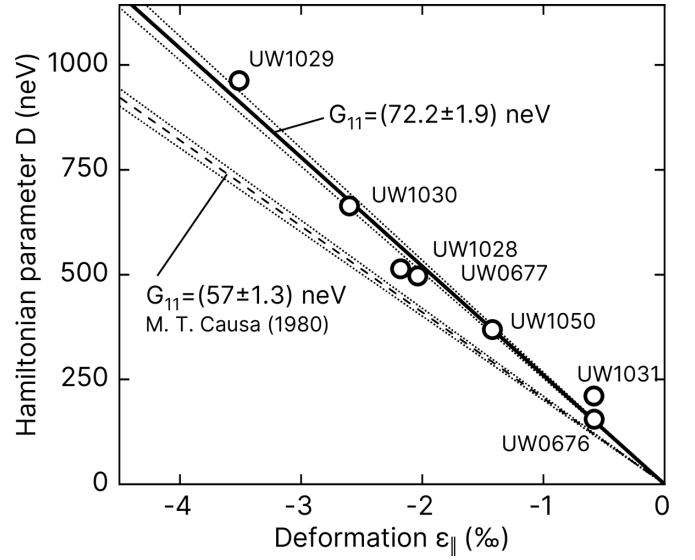

FIG. 12. The spin Hamiltonian D parameter obtained from angular ODMR measurements as a function of deformation for analyzed quantum well samples (circles). The dashed curve represents the value of G_{11} for bulk CdMnTe reported in Ref. [5]. The solid black curve represents the linear fit to data points measured in this work for Mn^{2+} in CdTe and corresponds to $G_{11} = (72.2 \pm 1.9)$ neV. The dotted lines represent one standard error deviation.

III. SUMMARY AND CONCLUSIONS

We have presented a precise method of determination of spin Hamiltonian parameters by angular-resolved ODMR measurements. Due to the high sensitivity of ODMR measurements (we were probing $\approx 3.8 \times 10^9$ manganese spins, which are almost 3 orders of magnitude less than the limit for standard EPR setup) we obtained strain-induced axial-symmetry spin Hamiltonian parameter D for single-layered quantum wells of 10-nm thickness with neV accuracy. By determination of D values for a series of samples differing by magnesium content, we were able to determine the strain spin-lattice coefficient $G_{11} = (72.2 \pm 1.9)$ neV for Mn^{2+} ion in CdTe.
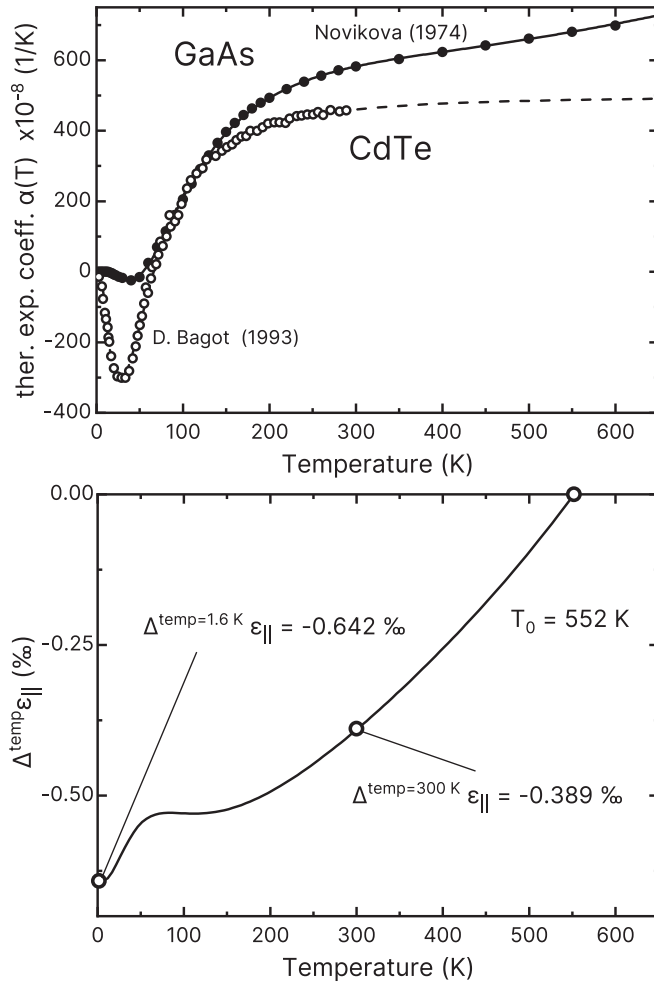
FIG. 13. The upper panel presents linear thermal expansion coefficients of CdTe and GaAs as a function of temperature. Data for CdTe and GaAs were taken from Bagot *et al.* [77] and Novikova *et al.* [76], respectively. Curves are best-fit results of fitting Eq. (A2) to the data. The lower panel shows calculation results of the additional deformation $\Delta\varepsilon_\parallel^{\text{temp.}}$ present in the QW samples due to the difference in thermal expansion coefficients of CdTe material and GaAs substrate material. The T_0 is the temperature related to the MBE growth process.

APPENDIX A: TEMPERATURE DEPENDENCE OF THE THERMAL EXPANSION COEFFICIENTS OF CdTe AND GaAs

The substrate material of analyzed samples is made of GaAs on top of which a thick CdTe layer is deposited. As the CdTe is deposited at a temperature of around 560 K, the XRD measurements are performed at 300 K and optical measurements at 1.6 K it is crucial to take into account the mechanical properties of the samples. In fact, the presented design is an example of composite-material behaving similarly to the bimetallic strip, as the thermal expansion coefficients α of GaAs and CdTe are different. Moreover, the changes of thermal expansion coefficient of both materials—$\alpha(T)$, as the temperature changes, are different. As a result, accumulated deformation, due to the cooling, must be evaluated based on full $\alpha(T)$ curves. The values of α are available in the literature

TABLE II. Numerical values of s_i and g_i coefficients used for reproduction of the linear thermal expansion coefficients $\alpha(T)$ of CdTe and GaAs with Eq. (A2).

Material	i	s_i (K)	g_i (K^{-1})
CdTe	1	222.02098	883.96417
	2	−40.90023	−384.86715
	3	−13241.61	1403.50696
GaAs	1	3562.24838	640.97475
	2	−99.54697	−44.50516
	3	371.47981	709.90672

for both CdTe [73–77] and GaAs [76,78–81]. The additional deformation present in CdTe layer can be then calculated as

$$\Delta\varepsilon_\parallel^{\text{temp.}} = \int_{T_0}^{T_i} [\alpha_{\text{GaAs}}(T) - \alpha_{\text{CdTe}}(T)]dT. \quad (A1)$$

For convenient integration, we interpolated literature data using an empirical formula:

$$\alpha(T) \approx \sum_{i=1}^{i=3} G_i(g_i, s_i, T), \quad (A2)$$

where

$$G_i(g_i, s_i, T) = g_i \left(\frac{s_i}{T}\right)^2 \frac{e^{\frac{s_i}{T}}}{\left(e^{\frac{s_i}{T}} - 1\right)^2}. \quad (A3)$$

Full theory and formulas are presented elsewhere [77]. However, only the combination of α curves from Ref. [77] for CdTe with Ref. [76] GaAs gives deformation value that agrees with values obtained from XRD measurements (see Table II and Fig. 13). As the temperature of the substrate during the MBE growth of the sample was known within 10 K accuracy we evaluate actual growth temperature T_0 as a value that results in the $\varepsilon_\parallel = -0.389‰$ measured with XRD. This procedure gives $T_0 = 552$ K. (See bottom panel of Fig. 13.)

APPENDIX B: TEMPERATURE DEPENDENCE OF THE CdTe ELASTIC STIFFNESS CONSTANTS

R. D. Greenough and S. B. Palmer in Ref. [82] presented experimentally determined linear combinations of the CdTe elastic parameters values from 300 to 4.2 K. From their data, one can calculate $2C_{12}/C_{11}$ ratio. In this paper, we evaluate $2C_{12}/C_{11}$ ratio using two components of Eq. (A2) and added constant C_0. We obtain the best reproduction of data from Ref. [82] for $g_1 = -0.0092$ K^{-1}, $g_2 = -0.015$ K^{-1}, $s_1 = -516$ K, $s_2 = 1415$ K, and $C_0 = 1.39886$. For temperatures below 50 K, as the temperature decreases, the value of C_0 approaches the $2C_{12}/C_{11}$ ratio. For 300 and 1.6 K, we find $2C_{12}/C_{11}|_{300\text{ K}} = 1.38859$ and $2C_{12}/C_{11}|_{1.6\text{ K}} = 1.39886$.

APPENDIX C: NUMERICAL SIMULATION OF QW LEVELS

Theoretical calculations of energy levels in QWs were performed by solving a 1D Schrodinger equation of carrier

confined in the square quantum well. The effective masses in perpendicular direction are assumed $0.1m_0$, $0.63m_0$, and $0.13m_0$ for electron, heavy and light hole, respectively where m_0 is the free electron mass. The potential was obtained from composition profiles. The QW layer was composed of $Cd_{1-y}Mn_yTe$, sandwiched between the $Cd_{1-x}Mg_xTe$ barriers, the chemical potential A_C and A_V for the conduction and valence bands is defined by the energy gap difference with a relative valence band offset $Q_V = 0.4$ [83].

We used a band gap versus composition relation [84]:

$$E_g^{Cd_{1-x}Mg_xTe}(x) = Bx + E_g^{CdTe} = (1.850x + 1.606) \text{ eV}, \quad (C1)$$

for the barrier material and for the QW:

$$E_g^{Cd_{1-y}Mn_yTe}(y) = By + E_g^{CdTe} = (1.563y + 1.606) \text{ eV}. \quad (C2)$$

The difference of lattice constants of buffer and barrier layers [85] leads to the presence of additional deformation potential $A_i^{deform} = \alpha_i \varepsilon_\parallel$, where i = E, HH, LH denotes electrons, heavy and light holes, respectively. The α_i parameters are corresponding to the a' (hydrostatic deformation potential) and b (shear deformation potential) material constants and elastic constants ratio. For zinc-blend crystals, as CdTe, the modified potential depths for the electrons, heavy and light holes are [48]

$$A_E = A_C + A_E^{deform} = A_C + \frac{2a'}{3}\left(2 - \frac{2C_{12}}{C_{11}}\right)\varepsilon_\parallel, \quad (C3)$$

$$A_{HH,LH} = A_V + A_{HH,LH}^{deform}$$
$$= A_V + \left[-\frac{a'}{3}\left(2 - \frac{2C_{12}}{C_{11}}\right) \pm b\left(1 + \frac{2C_{12}}{C_{11}}\right)\right]\varepsilon_\parallel. \quad (C4)$$

The elastic constants C_{12} and C_{11} are taken from literature [82], for this calculation we have used $2C_{12}/C_{11} = 1.39886$, while the parameter $a' = -3.85$ eV [9]. The light-heavy hole potential difference corresponds only to the difference in the deformation potential [see Eq. (1)].

The shear deformation potential $b = (-0.94 \pm 0.11)$ eV was obtained from the linear fit to the measured light-heavy hole splitting versus calculated $\varepsilon_\parallel$ as it was mentioned before. The exciton binding energy for heavy hole exciton was set as 18 meV, while for light hole exciton 21 meV, evaluated from the literature [33,86,87]. The QW width was equal to 10.45 nm, the same for each studied sample. With these assumptions, we have calculated heavy and light hole exciton energy levels and their energy difference presented in Fig. 6. Finally, the deformation $\varepsilon_\parallel$ splits heavy and light hole exciton energy levels.

Here we assume that the other parameters as the QW width and exciton binding energy are not vulnerable to the deformation. Moreover, the QW width, deformation potential corresponding to the a' parameter, and the exciton binding energy affect the exciton energy in a similar way—increasing or decreasing the state energy. Nonetheless, this additional energy offset does not affect the heavy-light hole splitting strain dependence which we are interested in here.

[1] C. Kolm, S. A. Kulin, and B. L. Averbach, Phys. Rev. **108**, 965 (1957).

[2] I. C. Bassignana, D. A. Macquistan, G. C. Hillier, R. Streater, D. Beckett, A. Majeed, and C. Miner, J. Cryst. Growth **178**, 445 (1997).

[3] K. Usuda and M. Ando, J. Appl. Phys. **80**, 1352 (1996).

[4] M. Qazzaz, G. Yang, S. H. Xin, L. Montes, H. Luo, and J. K. Furdyna, Solid State Commun. **96**, 405 (1995).

[5] M. T. Causa and M. Tovar, Phys. Lett. **77**, 473 (1980).

[6] Y. Merle d'Aubigné, H. Mariette, N. Magnea, H. Tuffigo, R. Cox, G. Lentz, L. Dang, J. Pautrat, and A. Wasiela, J. Cryst. Growth **101**, 650 (1990).

[7] D. G. Thomas, J. Appl. Phys. **32**, 2298 (1961).

[8] H. Mathieu, J. Allegre, A. Chatt, P. Lefebvre, and J. P. Faurie, Phys. Rev. B **38**, 7740 (1988).

[9] P. Peyla, Y. Merle d'Aubigné, A. Wasiela, R. Romestain, H. Mariette, M. D. Sturge, N. Magnea, and H. Tuffigo, Phys. Rev. B **46**, 1557 (1992).

[10] R. V. Cherbunin, V. M. Litviak, I. I. Ryzhov, A. V. Koudinov, S. Elsässer, A. Knapp, T. Kiessling, J. Geurts, S. Chusnutdinow, T. Wojtowicz, and G. Karczewski, Phys. Rev. B **101**, 241301(R) (2020).

[11] A. Lafuente-Sampietro, H. Boukari, and L. Besombes, Phys. Rev. B **95**, 245308 (2017).

[12] I. V. Dinu, V. Moldoveanu, R. Dragomir, and B. Tanatar, Phys. Status Solidi B **254**, 1600800 (2017).

[13] V. Moldoveanu, I. V. Dinu, R. Dragomir, and B. Tanatar, Phys. Rev. B **93**, 165421 (2016).

[14] A. Lafuente-Sampietro, H. Boukari, and L. Besombes, Phys. Status Solidi C **13**, 546 (2016).

[15] A. Lafuente-Sampietro, H. Boukari, and L. Besombes, Phys. Rev. B **92**, 081305(R) (2015).

[16] M. Goryca, M. Koperski, T. Smoleński, Ł. Cywiński, P. Wojnar, P. Plochocka, M. Potemski, and P. Kossacki, Phys. Rev. B **92**, 045412 (2015).

[17] S. Cronenberger, D. Scalbert, D. Ferrand, H. Boukari, and J. Cibert, Nat. Commun. **6**, 8121 (2015).

[18] J. Kobak, T. Smoleński, M. Goryca, M. Papaj, K. Gietka, A. Bogucki, M. Koperski, J.-G. Rousset, J. Suffczyński, E. Janik, M. Nawrocki, A. Golnik, P. Kossacki, and W. Pacuski, Nat. Commun. **5** (2014).

[19] B. Varghese, H. Boukari, and L. Besombes, Phys. Rev. B **90**, 115307 (2014).

[20] L. Besombes and H. Boukari, Phys. Rev. B **89**, 085315 (2014).

[21] M. Goryca, M. Koperski, P. Wojnar, T. Smoleński, T. Kazimierczuk, A. Golnik, and P. Kossacki, Phys. Rev. Lett. **113**, 227202 (2014).

[22] S. Cronenberger, M. Vladimirova, S. V. Andreev, M. B. Lifshits, and D. Scalbert, Phys. Rev. Lett. **110**, 077403 (2013).

[23] S. Jamet, H. Boukari, and L. Besombes, Phys. Rev. B **87**, 245306 (2013).

[24] Y. S. Chen, M. Wiater, G. Karczewski, T. Wojtowicz, and G. Bacher, Phys. Rev. B **87**, 155301 (2013).

[25] L. Besombes, C. L. Cao, S. Jamet, H. Boukari, and J. Fernández-Rossier, Phys. Rev. B **86**, 165306 (2012).

[26] M. Goryca, T. Kazimierczuk, M. Nawrocki, A. Golnik, J. A. Gaj, P. Kossacki, P. Wojnar, and G. Karczewski, Phys. Rev. Lett. **103**, 087401 (2009).

[27] M. Goryca, D. Ferrand, P. Kossacki, M. Nawrocki, W. Pacuski, W. Maślana, J. A. Gaj, S. Tatarenko, J. Cibert, T. Wojtowicz, and G. Karczewski, Phys. Rev. Lett. **102**, 046408 (2009).

[28] C. Le Gall, L. Besombes, H. Boukari, R. Kolodka, J. Cibert, and H. Mariette, Phys. Rev. Lett. **102**, 127402 (2009).

[29] J. M. Hartmann, J. Cibert, F. Kany, H. Mariette, M. Charleux, P. Alleysson, R. Langer, and G. Feuillet, J. Appl. Phys. **80**, 6257 (1996).

[30] E. G. LeBlanc, M. Edirisooriya, O. S. Ogedengbe, O. C. Noriega, P. A. R. D. Jayathilaka, S. Rab, C. H. Swartz, D. R. Diercks, G. L. Burton, B. P. Gorman, A. Wang, T. M. Barnes, and T. H. Myers, J. Electron. Mater. **46**, 5379 (2017).

[31] J. Cibert, Y. Gobil, L. S. Dang, S. Tatarenko, G. Feuillet, P. H. Jouneau, and K. Saminadayar, Appl. Phys. Lett. **56**, 292 (1990).

[32] J. Cibert, R. André, C. Deshayes, G. Feuillet, P. H. Jouneau, L. S. Dang, R. Mallard, A. Nahmani, K. Saminadayar, and S. Tatarenko, Superlattices Microstruct. **9**, 271 (1991).

[33] J. A. Gaj, W. Grieshaber, C. Bodin-Deshayes, J. Cibert, G. Feuillet, Y. Merle d'Aubigné, and A. Wasiela, Phys. Rev. B **50**, 5512 (1994).

[34] A. Waag, H. Heinke, S. Scholl, C. R. Becker, and G. Landwehr, J. Cryst. Growth **131**, 607 (1993).

[35] P. Kossacki, N. The Khoi, J. A. Gaj, M. Kutrowski, M. Surma, G. Karczewski, T. Wojtowicz, and M. Guziewicz, Solid State Commun. **103**, 619 (1997).

[36] P. Kossacki, J. Phys.: Condens. Matter **15**, R471 (2003).

[37] P. Kossacki, H. Boukari, M. Bertolini, D. Ferrand, J. Cibert, S. Tatarenko, J. A. Gaj, B. Deveaud, V. Ciulin, and M. Potemski, Phys. Rev. B **70**, 195337 (2004).

[38] J. Allègre, B. Gil, J. Calatayud, and H. Mathieu, J. Cryst. Growth **101**, 603 (1990).

[39] M. S. Boley, R. J. Thomas, M. Chandrasekhar, H. R. Chandrasekhar, A. K. Ramdas, M. Kobayashi, and R. L. Gunshor, J. Appl. Phys. **74**, 4136 (1993).

[40] A. K. Bhattacharjee and G. Fishman, J. Cryst. Growth **184-185**, 942 (1998).

[41] A. Pajaczkowska, Prog. Cryst. Growth Charact. **1**, 289 (1978).

[42] E. Janik, E. Dynowska, J. Bąk-Misiuk, M. Leszczyński, W. Szuszkiewicz, T. Wojtowicz, G. Karczewski, A. Zakrzewski, and J. Kossut, Thin Solid Films **267**, 74 (1995).

[43] R. J. Baird, H. Holloway, M. A. Tamor, M. D. Hurley, and W. C. Vassell, J. Appl. Phys. **69**, 226 (1991).

[44] R. D. Horning and J.-L. Staudenmann, Appl. Phys. Lett. **50**, 1482 (1987).

[45] H. Tatsuoka, H. Kuwabara, H. Fujiyasu, and Y. Nakanishi, J. Appl. Phys. **65**, 2073 (1989).

[46] H. Tatsuoka, H. Kuwabara, Y. Nakanishi, and H. Fujiyasu, J. Appl. Phys. **67**, 6860 (1990).

[47] H. Tatsuoka, H. Kuwabara, Y. Nakanishi, and H. Fujiyasu, Thin Solid Films **201**, 59 (1991).

[48] S. L. Chuang, *Physics of Photonic Devices*, 2nd ed., Wiley Series in Pure and Applied Optics (Wiley, Hoboken, N.J, 2009).

[49] S. J. C. H. M. van Gisbergen, M. Godlewski, R. R. Gałązka, T. Gregorkiewicz, C. A. J. Ammerlaan, and N. T. Khoi, Phys. Rev. B **48**, 11767 (1993).

[50] V. Ivanov, M. Godlewski, S. Yatsunenko, A. Khachapuridze, M. Li, and Z. Gołacki, Acta Phys. Pol. A **100**, 351 (2001).

[51] M. Godlewski, V. Y. Ivanov, A. Khachapuridze, and S. Yatsunenko, Phys. Status Solidi B **229**, 533 (2002).

[52] A. Khachapuridze, V. Ivanov, M. Godlewski, and G. Karczewski, Acta Phys. Pol. A **102**, 643 (2002).

[53] M. Godlewski, S. Yatsunenko, A. Khachapuridze, V. Y. Ivanov, Z. Gołacki, G. Karczewski, P. J. Bergman, P. J. Klar, W. Heimbrodt, and M. R. Phillips, J. Alloys Compd. **380**, 45 (2004).

[54] L. C. Smith, S. J. Bingham, J. J. Davies, and D. Wolverson, Appl. Phys. Lett. **87**, 202101 (2005).

[55] M. Godlewski, V. Y. Ivanov, and S. Yatsunenko, Opt. Mater. (Amsterdam) **30**, 669 (2008).

[56] P. G. Baranov, N. G. Romanov, D. O. Tolmachev, R. A. Babunts, B. R. Namozov, Y. G. Kusrayev, I. V. Sedova, S. V. Sorokin, and S. V. Ivanov, JETP Lett. **88**, 631 (2009).

[57] J. Debus, V. Y. Ivanov, S. M. Ryabchenko, D. R. Yakovlev, A. A. Maksimov, Y. G. Semenov, D. Braukmann, J. Rautert, U. Löw, M. Godlewski, A. Waag, and M. Bayer, Phys. Rev. B **93**, 195307 (2016).

[58] D. O. Tolmachev, V. Yu. Ivanov, D. R. Yakovlev, E. V. Shornikova, B. Witkowski, S. Shendre, F. Isik, S. Delikani, H. Volkan Demir, and M. Bayer, Nanoscale **12**, 21932 (2020).

[59] E. V. Shornikova, D. R. Yakovlev, D. O. Tolmachev, V. Y. Ivanov, I. V. Kalitukha, V. F. Sapega, D. Kudlacik, Y. G. Kusrayev, A. A. Golovatenko, S. Shendre, S. Delikanli, H. V. Demir, and M. Bayer, ACS Nano **14**, 9032 (2020).

[60] A. V. Komarov, S. Ryabchenko, O. Terletskii, and I. Zheru, J. Exp. Theor. Phys. **46**, 318 (1977).

[61] V. Y. Ivanov, M. Godlewski, D. R. Yakovlev, M. K. Kneip, M. Bayer, S. M. Ryabchenko, and A. Waag, Phys. Rev. B **78**, 085322 (2008).

[62] V. Y. Ivanov and M. Godlewski, Appl. Magn. Reson. **39**, 31 (2010).

[63] M. L. Sadowski, M. Byszewski, M. Potemski, A. Sachrajda, and G. Karczewski, Appl. Phys. Lett. **82**, 3719 (2003).

[64] M. Byszewski, D. Plantier, M. Sadowski, M. Potemski, A. Sachrajda, Z. Wilamowski, and G. Karczewski, Phys. E **22**, 652 (2004).

[65] D. O. Tolmachev, R. A. Babunts, N. G. Romanov, P. G. Baranov, B. R. Namozov, Y. G. Kusrayev, S. Lee, M. Dobrowolska, and J. K. Furdyna, Phys. Status Solidi B **247**, 1511 (2010).

[66] D. O. Tolmachev, A. S. Gurin, N. G. Romanov, A. G. Badalyan, R. A. Babunts, P. G. Baranov, B. R. Namozov, and Y. G. Kusrayev, JETP Lett. **96**, 231 (2012).

[67] A. S. Gurin, D. O. Tolmachev, N. G. Romanov, B. R. Namozov, P. G. Baranov, Y. G. Kusrayev, and G. Karczewski, JETP Lett. **102**, 230 (2015).

[68] D. Keller, D. R. Yakovlev, B. König, W. Ossau, T. Gruber, A. Waag, L. W. Molenkamp, and A. V. Scherbakov, Phys. Rev. B **65**, 035313 (2001).

[69] J. Seufert, G. Bacher, M. Scheibner, A. Forchel, S. Lee, M. Dobrowolska, and J. K. Furdyna, Phys. Rev. Lett. **88**, 027402 (2001).

[70] D. R. Yakovlev, M. Kneip, A. A. Maksimov, I. I. Tartakovskii, M. Bayer, D. Keller, W. Ossau, L. W. Molenkamp, A. V. Scherbakov, A. V. Akimov, and A. Waag, Phys. Status Solidi C **1**, 989 (2004).

[71] A. Hundt, J. Puls, A. V. Akimov, Y. H. Fan, and F. Henneberger, Phys. Rev. B **72**, 033304 (2005).

[72] A. Abragam and B. Bleaney, *Electron Paramagnetic Resonance of Transition Ions*, Oxford Classic Texts in the Physical Sciences (Oxford University Press, Oxford, 2012).

[73] S. Novikova, Fiz. Tverd. Tela **2**, 2341 (1960).

[74] M. Williams, R. Tomlinson, and M. Hampshire, Solid State Commun. **7**, 1831 (1969).

[75] J. S. Browder and S. S. Ballard, Appl. Opt. **11**, 841 (1972).

[76] S. Novikova, *Teplovoe Rasshirenie Tverdyh Tel* (Academy of Sciences of the Soviet Union, Nauka, Moscow, 1974).

[77] D. Bagot, R. Granger, and S. Rolland, Phys. Status Solidi B **177**, 295 (1993).

[78] P. W. Sparks and C. A. Swenson, Phys. Rev. **163**, 779 (1967).

[79] R. Feder and T. Light, J. Appl. Phys. **39**, 4870 (1968).

[80] T. Soma, J. Satoh, and H. Matsuo, Solid State Commun. **42**, 889 (1982).

[81] N. N. Sirota, A. M. Antyukhov, and A. A. Sidorov, Doklady Akademii Nauk SSSR **277**, 1379 (1984).

[82] R. D. Greenough and S. B. Palmer, J. Phys. D **6**, 587 (1973).

[83] T. Wojtowicz, M. Kutrowski, M. Surma, K. Kopalko, G. Karczewski, J. Kossut, M. Godlewski, P. Kossacki, and N. The Khoi, Appl. Phys. Lett. **68**, 3326 (1996).

[84] *Introduction to the Physics of Diluted Magnetic Semiconductors*, edited by J. A. Gaj and J. Kossut, Springer Series in Materials Science (Springer-Verlag, Berlin Heidelberg, 2010).

[85] E. Dynowska, E. Janik, J. Bąk-Misiuk, J. Domagała, T. Wojtowicz, and J. Kossut, J. Alloys Compd. **286**, 276 (1999).

[86] H. Mathieu, P. Lefebvre, and P. Christol, Phys. Rev. B **46**, 4092 (1992).

[87] P. Christol, P. Lefebvre, and H. Mathieu, J. Appl. Phys. **74**, 5626 (1993).